Predictor Laws for Pictorial Flight Displays

Arthur J. Grunwald*
Technion, Israel Institute of Technology, Haifa, Israel

Two predictor laws are formulated and analyzed: 1) a circular path law based on constant accelerations perpendicular to the path and 2) a predictor law based on state transition matrix computations. It is shown that for both methods the predictor provides the essential lead zeros for the path-following task. However, in contrast to the circular path law, the state transition matrix law furnishes the system with additional zeros that entirely cancel out the higher-frequency poles of the vehicle dynamics. On the other hand, the circular path law yields a zero steady-state error in following a curved trajectory with a constant radius. A combined predictor law is suggested that utilizes the advantages of both methods. A simple analysis shows that the optimal prediction time mainly depends on the level of precision required in the path-following task, and guidelines for determining the optimal prediction time are given.

Nomenclature

A = system matrix
a_ℓ, a_v = lateral, vertical inertial acceleration perpendicular to vehicle path
a_1, a_2 = control input spectrum, gust disturbance spectrum break frequency
B = control matrix
C_0, D_0, E_0 = row vectors for computing a_ℓ
D = predictor distance
I = identity matrix
K_λ = pilot gain on perceived angular error λ
P_1, P_2 = row vectors for computing a_ℓ
p, p_g = roll rate, roll rate gust disturbance
R_ℓ, R_v = lateral, vertical vehicle path radius
r = yaw rate
s = Laplace operator
T_p = prediction time
t = actual time
u = vector of control inputs
$\vec{V}, V$ = velocity vector and magnitude
W = disturbance matrix
w = vector of disturbance inputs
x = vector of perturbed vehicle states
x_5, x_6 = lateral deviation speed, lateral deviation
x_b, y_b, z_b = body-axis coordinate system
x_i, y_i, z_i = inertial coordinate system (north-east-down)
y_d, z_d = lateral, vertical deviation from trajectory
β, β_g = sideslip angle, side gust disturbance
Γ, Λ, Ξ = first, second, third integral of state transition matrix
$\Delta y_d, \Delta\chi$ = lateral deviation difference, path-angle difference between f and ℓ prediction method
δ_a, δ_r = aileron, rudder deflection
δ_{a_c} = command input to augmented system
ϵ = lateral control error
λ = perceived angular error
λ_ℓ, λ_v = lateral, vertical displacement of vehicle symbol on screen
ν = arc of circular path, between present and predicted vehicle position
τ = time shift
Φ = state transition matrix
χ, ξ = lateral, vertical path angle
ψ, θ, ϕ = yaw, pitch, roll angle

Superscripts

c = circular path predictor law
f = full-order predictor law
ℓ = linearized circular path predictor law
$*, **$ = matrix generated with A^*, A^{**}; Eqs. (15a,b)

Introduction

IT is commonly recognized that predictive information, superimposed either on computer-generated pictorial flight displays or on the visual field by head-up displays, markedly contributes to improved system performance.[1-9] Earlier simulator studies with a tunnel display used in the curved approach-to-landing[10,11] have shown that a predictor symbol, superimposed on the tunnel image, predicting the vehicle position at a given time in advance, both furnishes the system with the necessary damping cues, and assists the pilot in coping with the trajectory curvature forcing function by providing the correct control command information.

Since for in-flight displays the predictive computations have to be performed onboard and in real time, with limited computational resources, efficient algorithms are essential. Ideally, at every instant of time, the future time response should be computed by solving the complete set of nonlinear equations of motion of the vehicle many times a second. This "fast-time model" technique was first implemented with analog computers, operating iteratively in an accelerated time scale.[1,2] However, it was recognized that approximate methods such as a Taylor series expansion[3] or a regression technique,[8] demanding far less computation resources, could be used as well.

In this paper two slightly different approximate methods are compared and analyzed. The first method assumes a circular predicted path and is therefore very well suited for following curved trajectories with constant radius sections. The second method utilizes the linearized vehicle dynamics through state transition matrix computations. Since the future values of control and disturbance inputs are not known, assumptions have to be made as how these inputs vary over the prediction span. The effectiveness of methods using sophisticated "exact" models is therefore questionable, since the quality of the prediction still depends on these assumptions. In this paper, it is assumed that the control and disturbance inputs decay exponentially over the prediction span. The time constants of the decay should be chosen in accordance with the power density spectrum of the input signals. This approach allows adapta-

Received Jan. 4, 1984; revision received Aug. 28, 1984.

*Senior Lecturer, Flight Control Systems Engineering, Department of Aeronautical Engineering.

tion of the prediction to the input signals and is easily incorporated in transition matrix computations. Finally, the two prediction methods are compared in a root-locus and digital simulation study, for the lateral path-following task. On the assumption of rapidly decaying input signals, both methods yield very similar results in the lower-frequency modes. However, in the higher-frequency modes, the state transition method yields better results.

Predictor Laws

A tunnel display configuration for a three-dimensional approach is shown in Fig. 1. The desired winding and descending three-dimensional approach path is presented to the pilot by the perspective view of a "tunnel in the sky." Superimposed on the tunnel image is a perspective vehicle symbol, of which the center of gravity indicates the predicted vehicle location T_p seconds in advance. The predicted vehicle location is a point on the predicted vehicle path, at distance $D = VT_p$ ahead of the vehicle, where V is the vehicle velocity. The predicted vehicle path is assumed to be tangential to the velocity vector of the vehicle $\vec{V}$. The projections of this path on the $x_i y_i$ locally level plane and on the $x_i z_i$ locally vertical plane are hereafter referred to as the lateral and the vertical vehicle path, respectively.

There exist various ways to compute the predicted vehicle location. Two different predictor laws are described hereafter.

Circular Path Predictor Law

A simple method for computing the lateral and vertical vehicle path is to assume that the inertial accelerations in lateral direction a_ℓ (locally level plane) and in vertical direction a_v (locally vertical plane), perpendicular to the path, remain constant over the prediction span. In that case, circular lateral and vertical vehicle paths are obtained, with instantaneous path radii $R_\ell(t)$ and $R_v(t)$, respectively. The corresponding lateral an vertical path angle rates $\dot{\chi}$ and $\dot{\xi}$ are computed from

$$\dot{\chi}(t) = a_\ell(t)/V \quad \text{and} \quad \dot{\xi}(t) = a_v(t)/V \tag{1}$$

respectively. The situation for the horizontal path is shown in Fig. 2. The actual lateral path angle and lateral deviation are denoted by $\chi(t)$ and $y_d(t)$, respectively, and their predicted values T_p seconds in the future by $\chi^c(t+T_p)$ and $y_d^c(t+T_p)$, respectively, where the superscript c indicates that the circular law is used. For relatively small trajectory intercept angle ψ, sideslip angle β, and path angle χ, $\chi^c(t+T_p)$ and $y_d^c(t+T_p)$ are given by

$$\chi^c(t+T_p) = \chi(t) + \nu(t) \tag{2}$$

$$y_d^c(t+T_p) = y_d(t) + D\chi(t) + D\frac{D/R_\ell(t)}{1+\sqrt{1-[D/R_\ell(t)]^2}} \tag{3}$$

where for relatively small angle ν,

$$D/R_\ell(t) \approx \nu(t) = T_p\dot{\chi}(t) \tag{4}$$

A suitable control law might be that the pilot minimizes the actual lateral deviation from the trajectory by minimizing the deviation of the predictor symbol from the reference trajectory. In that case the advantage of the simple law of Eqs. (2-4) is that in a steady coordinated turn the radius of the desired trajectory will become equal to the radius of the predicted vehicle path, which will enable a zero steady-state error in the lateral deviation.

For small ν, the third term in Eq. (3) can be linearized, which yields

$$y_d^\ell(t+T_p) = y_d(t) + D\chi(t) + \tfrac{1}{2}DT_p\dot{\chi}(t) \tag{5}$$

where the superscript ℓ indicates the linearized circular path prediction. Using the expression $\dot{y}_d(t) = V\chi(t)$, Eq. (5) becomes

$$y_d^\ell(t+T_p) = y_d(t) + T_p\dot{y}_d(t) + \tfrac{1}{2}T_p^2\ddot{y}_d(t) \tag{6}$$

which is a Taylor series expansion until the second derivative.

The vertical predictor law is identical to Eqs. (2-4). Since the descent profile does not usually include constantly curved sections, the vertical path angle ξ remains small. Therefore, for the prediction of the vertical deviation z_d, it is sufficient to use the linearized expression:

$$z_d^\ell(t+T_p) = z_d(t) + D\xi(t) + \tfrac{1}{2}DT_p\dot{\xi}(t) \tag{7}$$

It follows from Eqs. (6) and (7) that a control law, based on the deviation of the predictor symbol from the reference trajectory, will include a combination of position, rate, and acceleration information. Current operational three-dimensional and four-dimensional guidance systems used in commercial aviation employ a similar combination of states in their flight director laws. However, the tunnel display has the advantage that, in addition to the control error of Eqs. (6) and (7), the tunnel image itself provides pure positional and vehicle attitude information as well as a preview of the trajectory forcing function. The information necessary to draw the tunnel image is directly obtained from measurements of an Instrument Landing System (ILS) or Microwave Landing System (MLS) and of an onboard inertial platform or position gyros. In addition, the predictor symbol provides the damping cues. It is shown in the Appendix that the predictor motions can be computed directly from measurements of body mounted ac-

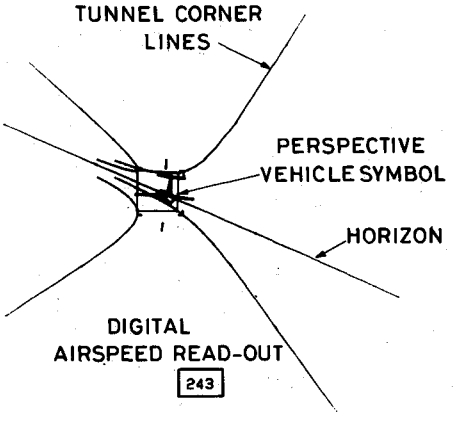

Fig. 1 Tunnel display with perspective vehicle symbol.

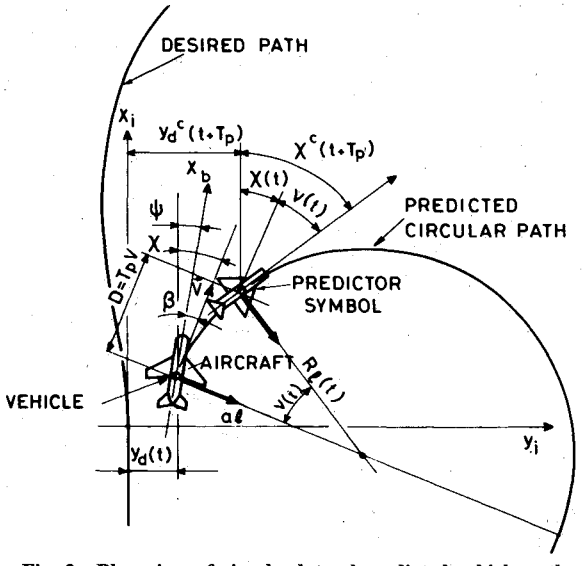

Fig. 2 Plan view of circular lateral predicted vehicle path.

celerometers, sideslip and angle-of-attack sensors, and a vertical gyro.

Full-Order Predictor Law

For small perturbations about a nominal trim condition, the linearized lateral or longitudinal vehicle dynamics can be described by the following state equation:

$$\dot{x}(t) = Ax(t) + Bu(t) + Ww(t) \tag{8}$$

where $x(t)$ is an m-dimensional vector of perturbed vehicle states; $u(t)$ an n-dimensional vector of control inputs; $w(t)$ an ℓ-dimensional vector of disturbances inputs; and A, B, and W the $(m\times m)$ system matrix, $(m\times n)$ control matrix, and $(m\times \ell)$ disturbance matrix, respectively. A linear prediction τ seconds in the future, from the present time t onward, is given by

$$x(t+\tau) = \Phi(\tau)x(t) + \int_{\sigma=0}^{\tau} \Phi(\sigma)Bu(t+\sigma)\mathrm{d}\sigma + \int_{\sigma=0}^{\tau} \Phi(\sigma)Ww(t+\sigma)\mathrm{d}\sigma \tag{9}$$

where $\Phi(\tau)$ is the transition matrix at τ of the system of Eq. (8). The prediction of Eq. (9) consists of three parts: The first term at the right-hand side constitutes the homogeneous system response, the second term constitutes the forced motion due to control commands, and the third term constitutes the forced motion due to external disturbances. Since the state of the vehicle $x(t)$ is, in most cases, available from measurements, or from a state estimator, the first term on the right-hand side of Eq. (9) can be computed directly from these measurements. However, the remaining terms depend on the future values of u and w, which are not known. Assuming $u(t)$ and $w(t)$ can be approximated by first-order Markov processes with break frequencies of a_1 and a_2 rad/s, respectively, then the least-squares optimal prediction is given by

$$u(t+\tau) = u(t)e^{-a_1\tau} \tag{10a}$$

and

$$w(t+\tau) = w(t)e^{-a_2\tau} \tag{10b}$$

Thus, a suitable assumption is that $u(t)$ and $w(t)$ decay exponentially over the prediction span. For a rapidly varying signal, e.g., very large values of a_1 or a_2, the future value of u or w is brought to zero quickly. On the other hand, for a slowly varying signal, e.g., very small values of a_1 or a_2, u or w remain almost constant over the prediction span. By substituting Eqs. (10a,b) into Eq. (9) and defining

$$\Gamma(\tau) = \int_{\sigma=0}^{\tau} \Phi(\sigma)\mathrm{d}\sigma \tag{11a}$$

$$\Gamma^*(\tau) = \int_{\sigma=0}^{\tau} \Phi(\sigma)e^{-a_1\sigma}\mathrm{d}\sigma \tag{11b}$$

$$\Gamma^{**}(\tau) = \int_{\sigma=0}^{\tau} \Phi(\sigma)e^{-a_2\sigma}\mathrm{d}\sigma \tag{11c}$$

Eq. (9) becomes

$$x(t+\tau) = \Phi(\tau)x(t) + \Gamma^*(\tau)Bu(t) + \Gamma^{**}(\tau)Ww(t) \tag{12}$$

where $\Phi(\tau)$ and $\Gamma(\tau)$ are given by the series expansions:

$$\Phi(\tau) = I + A\tau + A^2(\tau^2/2!) + \ldots + A^n(\tau^n/n!) + \ldots \tag{13}$$

$$\Gamma(\tau) = I\tau + A(\tau^2/2!) + A^2(\tau^3/3!) + \ldots + A^{n-1}(\tau^n/n!) + \ldots \tag{14}$$

where I is an identity matrix, and $\Gamma^*(\tau)$ and $\Gamma^{**}(\tau)$ are expanded according to Eq. (14) but with the matrix A replaced by

$$A^* = [A - a_1 I] \tag{15a}$$

and

$$A^{**} = [A - a_2 I] \tag{15b}$$

respectively.

The prediction given by Eq. (12) is elaborated hereafter for the lateral predictor motions. However, similar developments can be applied to the vertical predictor motions as well.

The linearized lateral dynamics, without stability augmentation systems and without integrations of the path geometry, is given in the Appendix and is written shortly as

$$\dot{x}_0(t) = A_0x_0(t) + B_0u(t) + W_0w(t) \tag{16}$$

where

$$x_0 \triangleq [x_1, x_2, x_3, x_4]^t \triangleq [\beta, p, \phi, r]^t \tag{17}$$

$$u \triangleq [u_1, u_2]^t \triangleq [\delta_a, \delta_r]^t \tag{18}$$

$$w \triangleq [w_1, w_2]^t \triangleq [\beta_g, p_g]^t \tag{19}$$

and where β is the sideslip angle, p the roll rate, ϕ the roll angle, r the yaw rate, δ_a and δ_r the aileron and rudder deflections, respectively, and β_g and p_g the gust disturbances. The lateral inertial acceleration a_ℓ is given by

$$a_\ell = V(\dot{\beta} + r) \tag{20}$$

which can be written as

$$a_\ell = P_1\dot{x}_0 + P_2x_0 \tag{21}$$

with

$$P_1 \triangleq [V\ 0\ 0\ 0] \tag{22a}$$

$$P_2 \triangleq [0\ 0\ 0\ V] \tag{22b}$$

Using Eq. (16), to eliminate $\dot{x}_0$ Eq. (21) can be written as

$$a_\ell = C_0x_0 + D_0u + E_0w \tag{23}$$

where

$$C_0 = P_1A_0 + P_2 \tag{24a}$$

$$D_0 = P_1B_0 \tag{24b}$$

$$E_0 = P_1W_0 \tag{24c}$$

The lateral deviation speed x_5 and lateral deviation x_6 are obtained by integration of a_ℓ and x_5, respectively. Adding these integrations to the system of Eq. (16) yields the following augmented system:

$$\begin{bmatrix} \dot{x}_0(t) \\ \hline \dot{x}_5(t) \\ \hline \dot{x}_6(t) \end{bmatrix} = \left[\begin{array}{c|c|c} A_0 & 0 & 0 \\ \hline C_0 & 0 & 0 \\ \hline 0 & 1 & 0 \end{array}\right] \begin{bmatrix} x_0(t) \\ \hline x_5(t) \\ \hline x_6(t) \end{bmatrix} + \begin{bmatrix} B_0 \\ \hline D_0 \\ \hline 0 \end{bmatrix} u(t) + \begin{bmatrix} W_0 \\ \hline E_0 \\ \hline 0 \end{bmatrix} w(t) \tag{25}$$

Using the system matrix of Eq. (25) in the series expansions of Eqs. (13) and (14) yields

$$\Phi(\tau)=\left[\begin{array}{c|c|c} \Phi_0(\tau) & 0 & 0 \\ \hline C_0\Gamma_0(\tau) & 1 & 0 \\ \hline C_0\Lambda_0(\tau) & \tau & 1 \end{array}\right] \tag{26a}$$

and

$$\Gamma(\tau)=\left[\begin{array}{c|c|c} \Gamma_0(\tau) & 0 & 0 \\ \hline C_0\Lambda_0(\tau) & \tau & 0 \\ \hline C_0\Xi_0(\tau) & \tau^2/2 & \tau \end{array}\right] \tag{26b}$$

where $\Phi_0(\tau)$ is the state transition matrix of A_0 at τ, and $\Gamma_0(\tau)$, $\Lambda_0(\tau)$, and $\Xi_0(\tau)$ are the first, second and third integrals of $\Phi_0(\tau)$, respectively, which are given by the following series expansions:

$$\Phi_0(\tau)\triangleq e^{A_0\tau}=I+A_0\tau+\ldots+A_0^n\frac{\tau^n}{n!}+\ldots \tag{27}$$

$$\Gamma_0(\tau)\triangleq\int_0^\tau\Phi_0(v)\mathrm{d}v=I\tau+A_0\frac{\tau^2}{2!}+\ldots +A_0^{n-1}\frac{\tau^n}{n!}+\ldots \tag{28}$$

$$\Lambda_0(\tau)\triangleq\int_0^\tau\Gamma_0(r)\mathrm{d}r=I\frac{\tau^2}{2!}+A_0\frac{\tau^3}{3!}+\ldots +A_0^{n-2}\frac{\tau^n}{n!}+\ldots \tag{29}$$

$$\Xi_0(\tau)\triangleq\int_0^\tau\Lambda_0(w)\mathrm{d}w=I\frac{\tau^3}{3!}+A_0\frac{\tau^3}{4!}+\ldots +A_0^{n-3}\frac{\tau^n}{n!}+\ldots \tag{30}$$

The matrices $\Gamma^*(\tau)$ and $\Gamma^{**}(\tau)$ are computed according to Eqs. (24a), (26b), (28), (29), and (30) with the matrix A_0 replaced by

$$A_0^*=A_0-a_1I \tag{31a}$$

and

$$A_0^{**}=A_0-a_2I \tag{31b}$$

respectively.

From Eqs. (27-30), the following useful relations can be derived:

$$\Lambda_0=A_0\Xi_0(\tau)+I(\tau^2/2!) \tag{32}$$

$$\Gamma_0(\tau)=A_0\Lambda_0(\tau)+I\tau \tag{33}$$

$$\Phi_0(\tau)=A_0\Gamma_0(\tau)+I \tag{34}$$

Using the expressions of Eqs. (26a,b) in Eq. (12) yields the predictions of the lateral speed of deviation x_5 and lateral deviation x_6, τ seconds in the future:

$$\chi^f(t+\tau)\triangleq x_5^f(t+\tau)=C_0\Gamma_0(\tau)x_0(t)+x_5(t) +C_0^*\Lambda_0^*(\tau)B_0u(t)+\tau D_0u(t) +C_0^{**}\Lambda_0^{**}(\tau)W_0w(t)+\tau E_0w(t) \tag{35}$$

and

$$y_d^f(t+\tau)\triangleq x_6^f(t+\tau)=C_0\Lambda_0(\tau)x_0(t)+\tau x_5(t)+x_6(t) +C_0^*\Xi_0^*(\tau)B_0u(t)+\tfrac{1}{2}\tau^2D_0u(t) +C_0^{**}\Xi_0^{**}(\tau)W_0w(t)+\tfrac{1}{2}\tau^2E_0w(t) \tag{36}$$

where the superscripts * and ** indicate that the corresponding matrix is generated with A_0^* and A_0^{**} of Eqs. (31a) and (31b), respectively, rather than with A_0. The superscript f indicates that the full-order predictor law is intended.

It is shown earlier that linearization of the circular path prediction yields the second-order Taylor series expansion of Eq. (6). With $\ddot{y}_d\triangleq a_l$; $\dot{y}_d\triangleq x_5$ and $y_d\triangleq x_6$, and, after substitution of Eq. (23), Eq. (6) becomes

$$y_d^\ell(t+\tau)\triangleq x_6^\ell(t+\tau)=C_0(\tau^2/2!)x_0(t)+\tau x_5(t)+x_6(t) +\tfrac{1}{2}\tau^2D_0u(t)+\tfrac{1}{2}\tau^2E_0w(t) \tag{37}$$

The difference between the two prediction methods is defined as

$$\Delta y_d(t+\tau)\triangleq\Delta x_6(t+\tau)\triangleq x_6^f(t+\tau)-x_6^\ell(t+\tau) \tag{38}$$

Subtracting Eq. (37) from Eq. (36) and using Eq. (32) yields

$$\Delta y_d(t+\tau)=C_0A_0\Xi_0(\tau)x_0(t) +C_0^*\Xi_0^*(\tau)B_0u(t)+C_0^{**}\Xi_0^{**}(\tau)W_0w(t) \tag{39}$$

Similarly, the circular path prediction of the lateral speed of deviation is approximated by

$$x_5^\ell(t+\tau)=x_5(t)+\tau\dot{x}_5(t) \tag{40}$$

Using Eq. (25), Eq. (40) is written as

$$x_5^\ell(t+\tau)=C_0\tau x_0(t)+x_5(t)+\tau D_0u(t)+\tau E_0w(t) \tag{41}$$

The difference in path angle between the two prediction methods is defined as

$$\Delta\chi(t+\tau)\triangleq(1/V)\Delta x_5(t+\tau)\triangleq(1/V)\left[x_5^f(t+\tau)-x_5^\ell(t+\tau)\right] \tag{42}$$

Subtracting Eq. (41) from Eq. (35) and using Eq. (33) yields

$$\Delta\chi(t+\tau)=(1/V)\left[C_0A_0\Lambda_0(\tau)x_0(t) +C_0^*\Lambda_0^*(\tau)B_0u(t)+C_0^{**}\Lambda_0^{**}(\tau)W_0w(t)\right] \tag{43}$$

The advantages of the nonlinear circular path prediction of Eqs. (2-4) and of the linear state transition matrix prediction of Eqs. (35) and (36) can be combined by adding the differences $\Delta\chi(t+\tau)$ and $\Delta y_d(t+\tau)$ to Eqs. (2) and (3). For $\tau=T_p$, this yields

$$\chi(t+T_p)=\chi^c(t+T_p)+\Delta\chi(t+T_p) \tag{44}$$

$$y_d(t+T_p)=y_d^c(t+T_p)+\Delta y_d(t+T_p) \tag{45}$$

This law combines the advantage of a zero steady-state error in constantly curved sections with the advantage of a full-order prediction given by the state transition matrix method.

Predictor Law Analysis

The lateral control error ϵ is defined as the lateral deviation of the predictor symbol from the reference trajectory. It is assumed that the pilot will bring the vehicle back on the

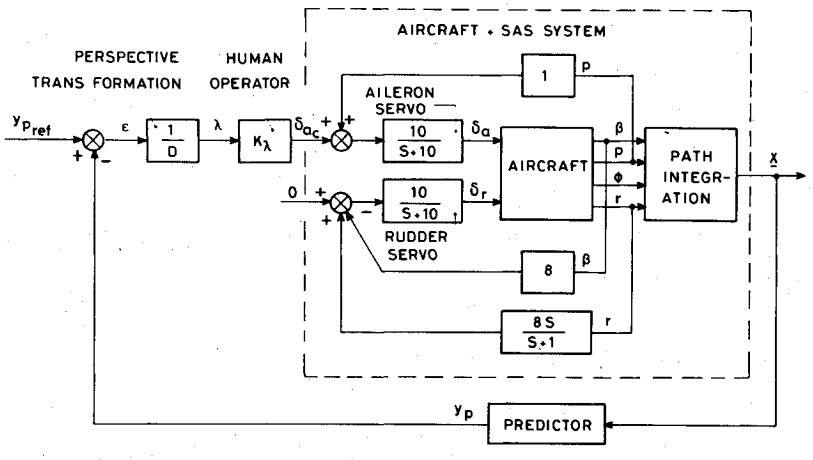

Fig. 3 Block diagram of pilot-vehicle system.

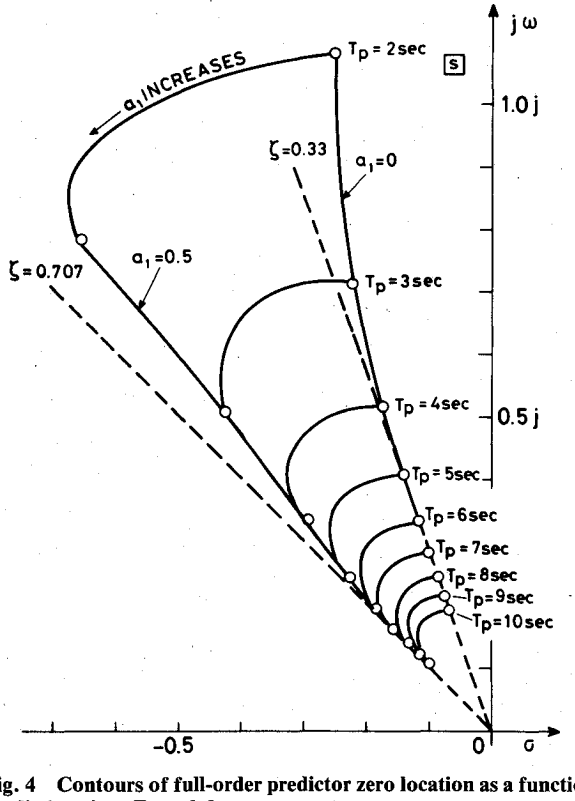

Fig. 4 Contours of full-order predictor zero location as a function of prediction time T_p and decay parameter a_1.

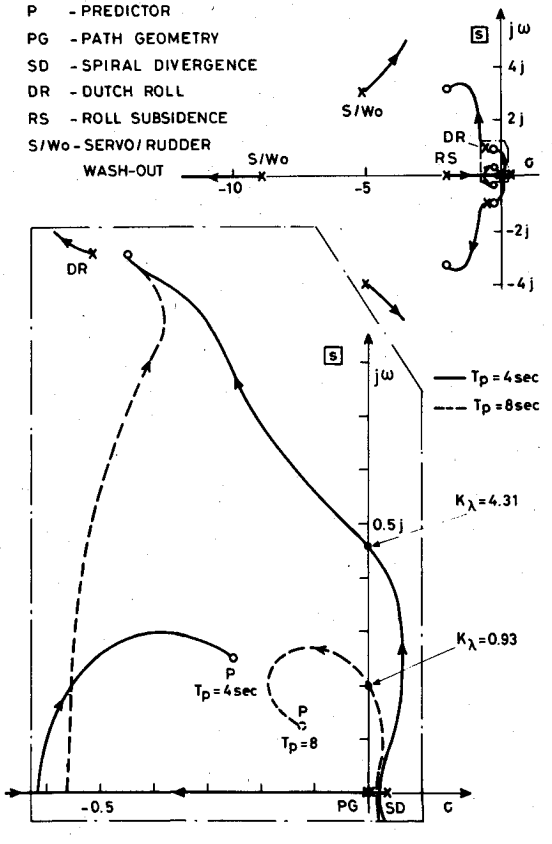

Fig. 5 Root-locus plot for lateral deviation control with second-order predictor.

reference trajectory by bringing ϵ to zero. A block diagram of the pilot-vehicle system is shown in Fig. 3. For simplicity it is assumed that the pilot acts as a simple gain on the perceived angular error $\lambda = \epsilon/D$ according to the control law: $\delta_{a_c} = K_\lambda \lambda$. In this simplified analysis, the pilot time-delay and neuromuscular lag are neglected. It is also assumed that the pilot does not produce lead compensation and that all the required compensation is produced by the dynamic characteristics of the predictor.

First, the second-order predictor law of Eq. (6) is considered. For simplicity, $y_d^\ell(t+T_p)$ is denoted by y_p^ℓ, and $y_d^f(t+T_p)$ by y_p^f. The transfer function $H^{y_p^\ell}_{\delta_{a_c}}(s)$ is identical to $H^{y_d^\ell}_{\delta_{a_c}}(s)$ except for the addition of a pair of complex zeros with a fixed damping ratio $\zeta = 0.707$ and a natural frequency inverse proportional to T_p according to $\omega_n = 1.414/T_p$. These zeros are a function of T_p only and are not influenced by the vehicle dynamics.

The transfer function $H^{y_d^f}_{\delta_{a_c}}(s)$ for the full-order predictor has a numerator and denominator of equal order (i.e., of order 9, for stability augmentation system engaged). Six of these zeros coincide with the poles of the characteristic equation, representing Dutch-roll mode, roll-subsidence, and stability augmentation system dynamics. One of the remaining zeros is real and two are complex; all of them located in the left half of the s plane. The complex zeros are equivalent to the predictor-path zeros of the second-order predictor. However, in contrast to the second-order predictor, these zeros depend on the vehicle dynamics, prediction time T_p, and decay parameter a_1. Contours of the location of these zeros as a function of T_p and a_1 are shown in Fig. (4). For $a_1 = 0\ s^{-1}$, i.e., the control command does not decay over the prediction span, the damping ratio is about $\xi = 0.33$ and decreases with decreasing prediction time. An increase in a_1, i.e., increased decay over the prediction span, improves the damping ratio. For $a = 0.5\ s^{-1}$, the damping ratio is similar to that for the second-order predictor.

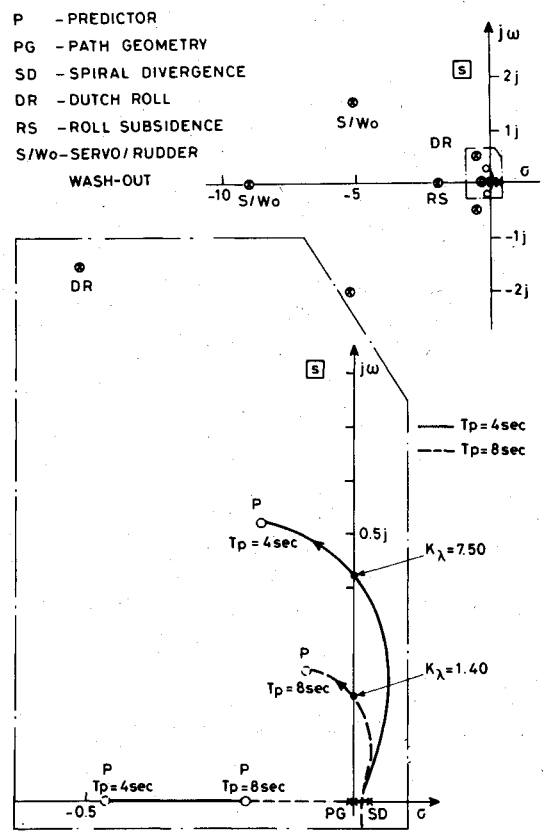

Fig. 6 Root-locus plot for lateral deviation control with full-order predictor, $a_1 = 0\ s^{-1}$.

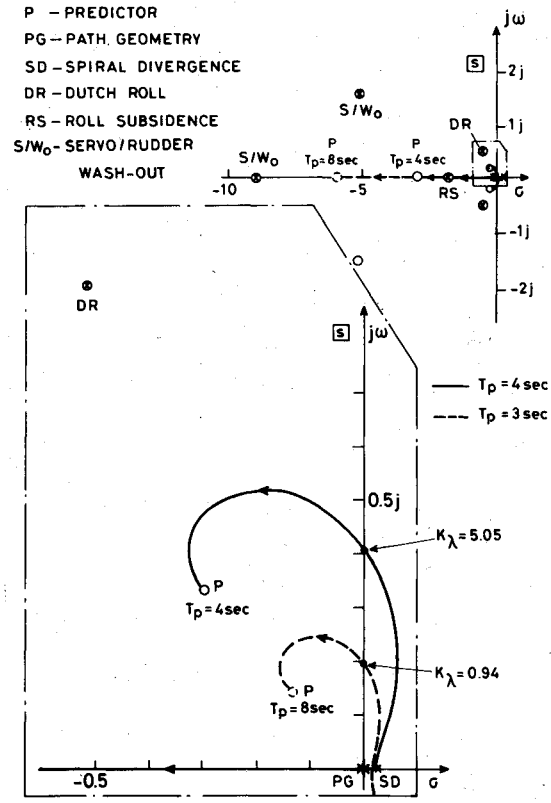

Fig. 7 Root-locus plot for lateral deviation control with full-order predictor, $a_1 = 0.5\ s^{-1}$.

Figure 5 shows a root-locus plot of the system with the second-order predictor. The plot in the upper right corner shows the reduced scale. It is clear that the predictor zeros are largely responsible for stabilizing the system. For $T_p = 8$ s, the loci departing from the spiral divergence pole and from one of the path geometry poles (dotted line) will terminate at the predictor zeros. A minimal gain of $K_\lambda = 0.93$ is required to stabilize the system. For $T_p = 4$ s, these loci arrive at the zeros associated with the Dutch-roll mode and the minimal gain to stabilize the system is much higher, i.e., $K_\lambda = 4.31$. The reduced-scale plot shows that the three poles of the stability augmentation system move outward along asymptotes of 60, −60, and 180 deg. For a high pilot gain this migh result in high-frequency oscillatory instability. However, under normal circumstances this high gain will not be reached.

Figure 6 shows the root-locus plot for the full-order predictor with $a_1 = 0\ s^{-1}$. In contrast with the second-order predictor, the higher-frequency poles of the system are cancelled out completely by six zeros of the predictor. Also, for the full-order predictor, the three remaining zeros are responsible for stabilizing the system. For $T_p = 8$ s, the minimal gain for obtaining stability is $K_\lambda = 1.40$ and, for $T_p = 4$ s, $K_\lambda = 7.50$, thus requiring a higher pilot gain than the second-order predictor. However, the basic difference with the second-order predictor is that the root-locus plot does not have asymptotes, so the high-frequency oscillatoric instability is not present.

Figure 7 shows the root-locus plot for the full-order predictor with $a_1 = 0.5\ s^{-1}$. The plot is identical to the one for $a_1 = 0\ s^{-1}$, except for the fact that the damping for high pilot-gain is much better. The minimal gain for obtaining stability is $K_\lambda = 0.94$ for $T_p = 8$ s and $K_\lambda = 5.05$ for $T_p = 4$ s. These values are lower than the ones for $a_1 = 0\ s^{-1}$.

The Choice of Predictor Distance

The root-locus plots of Figs. 5-7 show that, for a sufficiently high pilot gain, the dominant closed-loop system poles will be located at the predictor zeros. Thus, the closed-loop system bandwidth will increase with decreasing T_p, while the system damping remains more or less constant. However, the pilot-gain required to reach the zeros will drastically increase with decreasing T_p. This pilot-gain should be selected such that the closed-loop poles are sufficiently close to the zeros on one hand, and the control commands and vehicle motions remain within reasonable bounds on the other hand. Since with the proportional control law the control commands are proportional to the predicted lateral deviation, they highly depend on the actual lateral deviation as well. Therefore, the smaller the actual lateral deviation, the higher the allowed pilot-gain. In order to establish the relation between lateral deviation, prediction time, and pilot-gain, a series of computer simulations was carried out in which a straight reference trajectory was entered from an initial off-center location, while the initial vehicle heading angle and trajectory heading angle were equal. The second-order predictor was used. The results of these simulation runs are summarized in Fig. 8. The dotted lines establish the upper limit on K_λ for given $y_d(0)$ and as a function of T_p. This limit was chosen such that at all times the constraints $\phi \leq 30$ deg, $p \leq 1$ rad/s, and $\delta_a \leq 30$ deg were satisfied. The solid line establishes the minimal required pilot gain to obtain a stable system, as a function of T_p. Figure 8 shows that for a larger initial lateral deviation, i.e., $y_d(0) = 450$ ft, the minimal required prediction time is at least 6 s. For T_p less than 6 s, the minimal gain for stability will exceed the upper gain limit for $y_d(0) = 450$ ft. The dot-bar line indicates the "best choice" for the gain, as a function of T_p. It is the minimal gain required for the lateral deviation to settle within 5% of $y_d(0)$ within 60 s.

Figure 9 shows the curves for the "best choice" of T_p and K_λ as a function of $y_d(0)$. The initial lateral deviation $y_d(0)$ can be interpreted as the level of precision required for a particular task. Thus the graph of Fig. 9 shows that for given vehicle dynamics and velocity the "best choice" of T_p is a function of the task definition. For increasing level of precision, T_p reduces from 10 to 4 s.

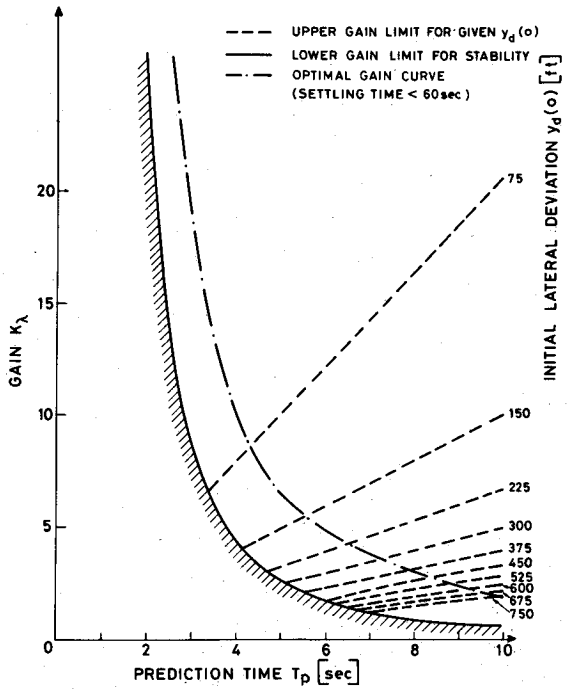

Fig. 8 Upper and lower pilot-gain limits as a function of prediction time T_p and initial lateral deviation y_d (0).

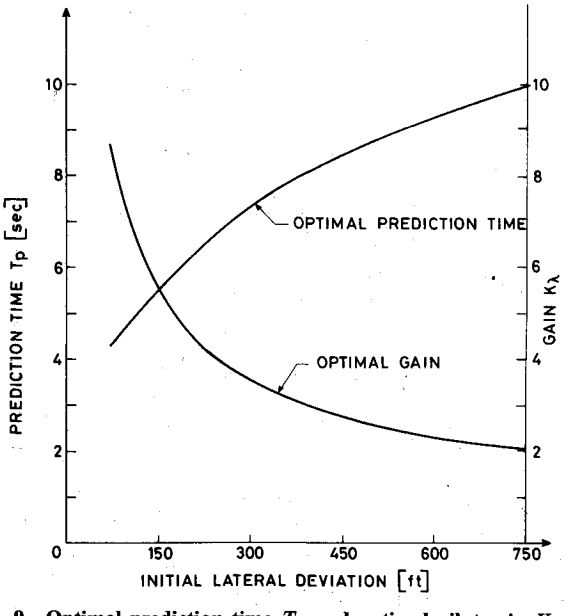

Fig. 9 Optimal prediction time T_p and optimal pilot-gain K_λ as a function of initial lateral deviation y_d(0).

Discussion

1) Both prediction methods provide the essential lead zeros for the path-following task.

2) For limited gain, the circular path or second-order predictor is basically equivalent to the full-order predictor. In cases in which computational resources are limited, the second-order predictor is recommended.

3) The full-order predictor yields zeros that coincide with higher-frequency vehicle dynamics poles. Therefore, for a higher gain, the full-order predictor is superior in the high-frequency modes.

4) The approach, assuming exponentially decaying input signals over the prediction span, allows adaptation of the prediction to these signals and is easily incorporated in the transition matrix computation.

5) The optimal predictor distance is subject to the required lateral accuracy.

6) The improvement obtained with sophisticated exact models is questionable, since the future input signals are not known.

Appendix

The linearized lateral equations of motion of the vehicle, for small deviations from the nominal trim condition, are given by

$$\begin{bmatrix} \dot{\beta} \\ \dot{p} \\ \dot{\phi} \\ \dot{r} \end{bmatrix} = \begin{bmatrix} Y_v & 0 & g/U_0 & -1 \\ L'_\beta & L'_p & 0 & L'_r \\ 0 & 1 & 0 & 0 \\ N'_\beta & N'_p & 0 & N'_r \end{bmatrix} \begin{bmatrix} \beta \\ p \\ \phi \\ r \end{bmatrix} + \begin{bmatrix} Y^*_{\delta_a} & Y^*_{\delta_r} \\ L'_{\delta_a} & L'_{\delta_r} \\ 0 & 0 \\ N'_{\delta_a} & N'_{\delta_r} \end{bmatrix} \begin{bmatrix} \delta_a \\ \delta_r \end{bmatrix} + \begin{bmatrix} -Y_v & 0 \\ -L'_\beta & -L'_p \\ 0 & 0 \\ -N'_\beta & -N'_p \end{bmatrix} \begin{bmatrix} \beta_g \\ p_g \end{bmatrix} \quad \text{(A1)}$$

where $Y^*_\delta = Y_\delta/U_0$, $\beta = v/U_0$, $\beta_g = v_g/U_0$, U_0 is the component of $\vec{V}$ in the x_b-body axis direction, g is the gravity acceleration, and the primed derivatives L'_i and N'_i are given by

$$L'_i = \frac{L_i + N_i J_{xz}/I_{xx}}{1 - J^2_{xz}/(I_{xx}/I_{zz})} \quad \text{(A2a)}$$

$$N'_i = \frac{N_i + L_i J_{xz}/I_{zz}}{1 - J^2_{xz}/(I_{xx}/I_{zz})} \quad \text{(A2b)}$$

where i can be β, p,r, δ_a, δ_r; and I_{xx}, I_{zz}, and J_{xz} are the vehicle moments of inertia about the x_b and z_b axis and product of inertia in the $x_b z_b$ plane, respectively. The stability derivative notation is $B_A = (1/C)(\partial B/\partial A)|_{\text{trim}}$, where B can be Y (total force in y_b axis direction), L (total rolling moment), or N (total yawing moment); A can be v, β, p, r, δ_a; δ_r; and C is m (vehicle mass) for Y, I_{xx} for L, and I_{zz} for N.

In this study, the stability derivatives of a DC-8 aircraft are chosen, in the approach-to-landing, trimmed at a nominal airspeed of 243.5 ft/s and with flaps extended to 35 deg. The dimensional stability derivatives are derived from Ref. 12. The lateral stability augmentation system includes a roll-rate on aileron feedback, a yaw-rate on rudder feedback with washout and a sideslip on rudder feedback. Aileron and rudder servo actuators are modeled by first-order lags with a 10.-rad/s break frequency. The equations of motion of this system are given by

$$\dot{\delta}_a = -10.0\delta_a + 10.0[1.0p + \delta_{a_c}] \quad \text{(A3)}$$

$$\dot{\delta}_r = -10.0\delta_r + 10.0[8.0r_w - 8.0\beta] \quad \text{(A4)}$$

$$\dot{r}_w = -1.0r_w + \dot{r} \quad \text{(A5)}$$

where r_w is the state of the washout filter, and δ_{a_c} is the command input to the system, originating from a lateral control stick motion. Turn coordination is accomplished by means of the sideslip on rudder feedback, which eliminates the need for a rudder command.

The lateral and vertical path accelerations a_ℓ and a_V can be computed from the specific forces measured by accelerometers in body axis direction $a^m_{x_b}$, $a^m_{y_b}$, $a^m_{z_b}$, by using vertical gyro measurements of pitch and roll angle. First, the inertial accelerations in body axis direction $a^i_{x_b}$, $a^i_{y_b}$, $a^i_{z_b}$ are computed

from

$$a^i_{x_b} = a^m_{x_b} - g\sin\theta \tag{A6}$$

$$a^i_{y_b} = a^m_{y_b} + g\cos\theta\sin\phi \tag{A7}$$

$$a^i_{z_b} = a^m_{z_b} + g\cos\theta\cos\phi \tag{A8}$$

Second, a_ℓ and a_v are computed from

$$a_\ell = a^i_{y_b}\cos\phi - a^i_{z_b}\sin\phi \tag{A9}$$

$$a_v = a^i_{y_b}\sin\phi + a^i_{z_b}\cos\phi \tag{A10}$$

The lateral displacement of the vehicle symbol on the display screen is equivalent to the lateral visual angle λ_ℓ at which the symbol is seen in the x_b, y_b, z_b body coordinate system, which is given by

$$\lambda_\ell(t) = \beta + \frac{D/R_\ell(t)}{1+\sqrt{1-[D/R_\ell(t)]^2}} \tag{A11}$$

with

$$D/R_\ell(t) = T_P a_\ell(t)/V \tag{A12}$$

Similarly, the vertical displacement λ_v of the vehicle symbol on the display screen is computed. In this case, the sideslip angle β is replaced by the angle-of-attack α, and the lateral path acceleration a_ℓ is replaced by the vertical acceleration a_v.

It is clear from Eqs. (A11) and (A12) that the variables necessary to position the predictor on the display are the outputs of vehicle mounted accelerometers, of a vertical gyro, and of sideslip and angle-of-attack sensors.

Acknowledgments

This research was sponsored by the National Aeronautics and Space Administration under Contract NASW-3302, under the technical direction of S.A. Morello of Langley Research Center, Hampton, Va. The author wishes to thank D. Shahar for his assistance in working out the computational examples.

References

[1]Kelley, C.R., "Developing and Testing the Effectiveness of the Predictor Instrument," Dunlap and Associates, Inc., Technical Rep. 252-60-1, March 7, 1960.

[2]Kelley, C.R., "Further Research on the Predictor Instrument," Dunlap and Associates Inc., Inglewood, Calif., Technical Rep. 252-60-2, Dec. 1960.

[3]Bernotat, R., "Das Prinzip der Voranzeige und Seine Anwendung in der Flugführung," *Zeitschrift für Flugwissenschaften,* Vol. 13, 1965, pp. 373-377.

[4]Warner, J.A., "A Fundamental Study of Predictive Display Systems," NASA CR-1274, 1969.

[5]Smith, R.L., Pence, G.G., Queen, J.E., and Wulfeck, J.W., "Effect of a Predictor Instrument on Learning to Land a Simulated Jet Trainer," Dunlap and Associates Inc., Inglewood, Calif., Aug. 1974.

[6]Smith, R.L. and Kennedy, R.S., "Predictor Displays: History, Research and Applications," Pacific Missile Test Center, Technical Publication 76-05, June 1975.

[7]Smith, R.L. and Kennedy, R.S., "Predictor Displays: A Human Engineering Technology in Search of a Manual Control Problem," Pacific Missile Test Center, Point Mugu, Calif., June 1976.

[8]Gallaher, P.D., Hunt, R.A., and Williges, R.C., "A Regression Approach to Generate Aircraft Predictor Information," 12th Annual Conference on Manual Control, NASA TM X-73, p. 170, 1976.

[9]Korn, J., Gully, S.W., and Kleinman, D.L., "Validation of an Advanced Cockpit Display Design Methodology via Workload/Monitoring Trade-off Analysis," 18th Annual Conference on Manual Control, AFWAL-TR-83-3021, June 1982, pp. 268-292.

[10]Grunwald, A.J., Robertson, J.B., and Hatfield, J.J., "Experimental Evaluation of a Perspective Tunnel Display for Three-Dimensional Helicopter Approaches," *Journal of Guidance and Control,* Vol. 4, Nov.-Dec. 1981, pp. 623-631.

[11]Grunwald, A.J., "Predictor Symbology in Computer-Generated Pictorial Displays," Technion Aeronautical Engineering Department, Technion, Haifa, Israel, TAE Rep. No. 470, Nov. 1981.

[12]McRuer, D., Ashkenas, I., and Graham, D., *Aircraft Dynamics and Automatic Control,* Princeton University Press, Princeton, N.J., 1973, pp. 711-717.